

COMMISSIONING OF THE BEAM ENERGY POSITION MONITORING SYSTEM FOR THE SUPERCONDUCTING RIKEN HEAVY-ION LINAC

T. Watanabe*, N. Fukunishi, H. Imao, O. Kamigaito, T. Nishi, K. Ozeki,
N. Sakamoto, A. Uchiyama, Y. Watanabe, K. Yamada, RIKEN, Wako, Japan
T. Toyama, KEK/J-PARC, Tokai, Japan
A. Kamoshida, National Instruments Japan Corporation, Tokyo, Japan
K. Hanamura, Mitsubishi Electric System & Service Co., Ltd., Tokai, Japan
R. Koyama, SHI Accelerator Service Ltd., Wako, Japan

Abstract

Beam commissioning for the RIKEN Heavy-ion Linac (RILAC) upgrade, including the new Superconducting Linac (SRILAC), has been successfully completed. The RILAC upgrade aims at promoting super-heavy element searches and radioactive isotope production for medical use. When the SRILAC beam is accelerated, the beam loss must be reduced to under 1 W/m. To continuously monitor the beam nondestructively, we have developed a new beam energy position monitoring (BEPM) system capable of simultaneously measuring the beam position and energy by measuring the time-of-flight. A great advantage of this system is that it can handle a time-chopped beam by synchronizing the measurement system with the beam-chopping signal. At the start of commissioning, the beam was chopped to 3% duty cycle to protect the SRILAC cavity from beam loss. Even though the beam intensity was 20 enA, we measured the beam position and energy to accuracies of ± 0.1 mm and several 10^{-4} precision, respectively. Here, we present details concerning the BEPM system and commissioning results.

INTRODUCTION

Nihonium (Nh) is a synthetic super-heavy (SH) element with atomic number 113 and is the first element ever discovered in Asia [1]. Its name comes from the word “Nihon”, which means “Japan” in Japanese. To promote the research for even heavier synthetic elements and to enhance the production capability of the short-lived radio isotope ^{211}At , which is expected to be useful in cancer therapy [2], an upgrade project of the RIKEN Heavy-ion Linac (RILAC) [3] has begun called the RI Beam Factory (RIBF) project [4, 5]. The project aims to increase the intensities and energies of the heavy ion beams by introducing a superconducting electron cyclotron resonance (ECR) ion source [6] and a superconducting booster named the Superconducting RILAC (SRILAC) [7].

In this scheme, it is crucial to monitor a beam to accelerate it stably. Destructive monitors generate outgassing; if they are used, it becomes difficult to maintain the Q value and surface resistance of the superconducting radio frequency (SRF) cavities over a long period of time. For this reason, we have developed a new beam energy and position monitoring (BEPM) system to continuously monitor the beam nondestructively.

* wtamaki@riken.jp

BEPM SYSTEM FOR THE SRILAC

RILAC and SRILAC

The newly constructed beam transport lines and the SRILAC were installed in February 2020. The existing RILAC and the upgraded facilities are shown in Fig 1. The SRILAC consists of three cryomodules (CM1, CM2, and CM3). CM1 and CM2 each contain four quarter-wavelength resonators (QWR) at 73 MHz and CM3 contains two QWRs. The total acceleration voltage is designed to produce 18 MW with a Q value of 1×10^9 . To maintain the ultra-high vacuum ($< 10^{-8}$ Pa) and particulate-free conditions, a non-evaporable getter-based differential pumping system was developed and installed upstream and down-stream of the SRILAC [8].

Heavy-ion beams accelerated by the SRILAC are used by the GAs-filled Recoil Ion Separator (GARIS) III to search for SH elements and to produce radioisotopes (RI) for medical use. If further acceleration is necessary in the future, the beams are to be transported to the rear stage Riken Ring Cyclotron (RRC).

Three Types of BEPMs

Depending on the installation location, 3 types of BEPM (Types I, II, and III) were designed and 11 BEPMs were fabricated [9] by Toyama Co., Ltd. [10]. BEPMs are installed in the centers of the quadrupole magnets (Fig. 1) that are located between the SRF cavities. Photographs of the 3 types

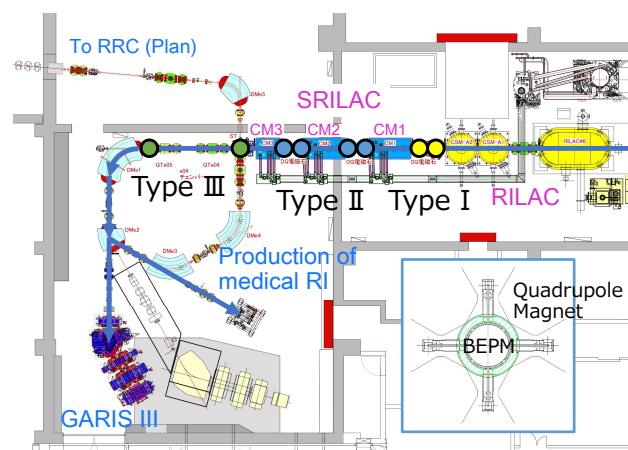


Figure 1: Schematic drawing of the RIKEN Heavy-ion Linac (RILAC), the upgraded Superconducting Linac (SRILAC), and the installation locations of the 3 types of BEPM.

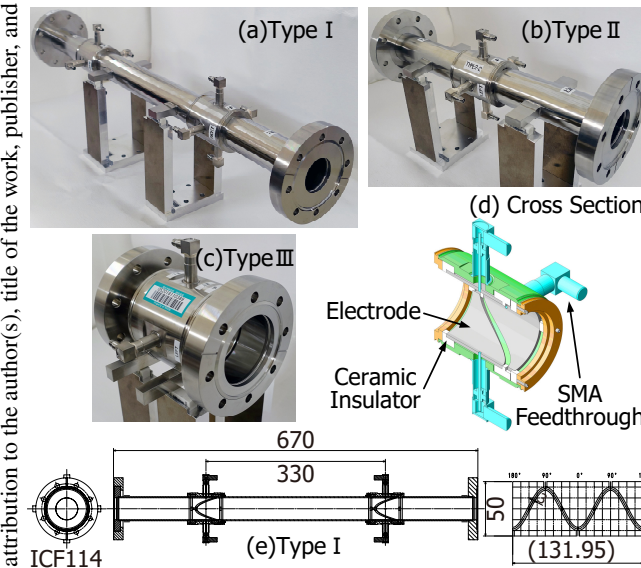


Figure 2: Photographs of the 3 types of BEPM: (a) Type I, (b) Type II, and (c) Type III. (d) Cross section drawing of a BEPM. (e) Schematic drawing of Type I.

of BEPMs and a cross section of a BEPM are shown in Fig. 2, and the mechanical dimensions of each type of BEPM are summarized in Table 1.

By using a parabolic design, the ideal linear response of the quadrupole moments is realized while maintaining good linear position sensitivity [11]. The shape of an electrode is represented by $y = (L/2) \cos 2\theta$, where θ is the angle in the cylindrical coordinate system, y is the longitudinal axis, and L is the length of the electrode. The electrode lengths were determined by taking into account both that the longitudinal distribution of the beam is $\pm 10\%$ of one period and the expansion of the electric field due to the non-affected Lorentz contraction.

Each BEPM has 4 reference planes in the x -axis direction and 8 in the y -axis direction. These reference planes are used for alignment and calibration; they are transferred from the center of the 4 electrodes, for which the mechanical accuracy is within ± 0.05 mm, while that of the other parts is within ± 0.1 mm. To confirm that the mechanical accuracy is maintained within the allowed values, after the welding process is completed, the reference planes are shaped again by using a milling cutter and remeasured by using a 3-D coordinate measuring machine. The vacuum chamber, electrode, and flange are made of super low carbon stainless steel

Table 1: Mechanical Dimensions (mm) of the 3 Types of BEPM

	Type I	Type II	Type III
Length of chamber	670	360	140
Outside dia. of chamber	58	58	85
Length of electrode	50	50	60
Inner dia. of electrode	40	40	60
Number of BEPMs	2	4	5

SUS316L, while the fixed and rotational flanges are made of ultra-high vacuum flange ICF114. To provide electrical insulation between each electrode and the vacuum chamber, an alumina ceramic (AS999 [12]) is used, which has a low $\tan\delta$ of 0.5×10^{-4} and a high purity of 99.99%. The signal induced on the electrode by the passing beam is sent outside the vacuum chamber via 50Ω SMA feed-throughs [13].

Analysis of the Pickup Signal in the Time and Frequency Domains

Before constructing the SRILAC BEPM system, we theoretically estimated the expected pickup signal in the time and frequency domains [14, 15]. Based on these estimations, a prototype BEPM system was designed, fabricated, and installed into the beam transport line at RIBF. By using a $17\text{ e}\mu\text{A}$ beam of $^{238}\text{U}^{64+}$ accelerated to 10.5 MeV/u by the RRC, the beam energy and position were measured for several months. The results showed that the agreement between the measured and theoretical values in the frequency domain and the bunch shape in the time domain, was satisfactory and confirmed that the system worked extremely well [16]. After this was established, we investigated the bunched beam signals from the electrostatic pickups of the SRILAC.

The equivalent circuit of an electrostatic pickup is shown in Fig. 3. When charged particles pass by a pickup, an induced voltage $V(t)$ is created over the input-resistance (R) of the amplifier. $V(t)$ is a solution of

$$\frac{dQ(t)}{dt} = \frac{V(t)}{R} + C \frac{dV(t)}{dt}, \quad (1)$$

where C is the total capacitance of the BEPM-electrode, feedthrough, and input of the amplifier. $V(t)$ and charge $Q(t)$ are expressed as $V(t) = V(\omega) \exp(j\omega t)$ and $Q(t) = Q(\omega) \exp(j\omega t)$, respectively. By substituting these equations into Eq. (1), the relationship between the voltage and the angular frequency becomes

$$V(\omega) = \frac{j\omega CR}{1+j\omega CR} \frac{Q(\omega)}{C}. \quad (2)$$

This circuit forms a high-pass filter with a time constant CR and cut-off frequency (f_c) given by

$$f_c = 1/(2\pi RC). \quad (3)$$

In this case, the cut-off frequency is calculated to be 74 MHz

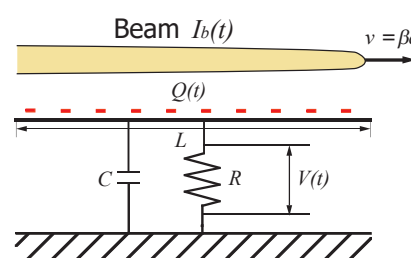


Figure 3: Equivalent circuit for an electrostatic pickup. A beam induces charge $Q(t)$ on the electrodes and voltage $V(t)$ appears on the input-resistance R of the preamplifier, where C is the capacitance of the BEPM-electrodes.

Table 2: Calculation Parameters

β	0.082	($\frac{51}{23}V^{13+}$ beam)
N	5.489×10^6	(2.469 pA)
q	13	Particle charge
T_0	13.699 ns	($f_{rf} = 73$ MHz)
σ	1.00 ns	Standard deviation
L	0.06 m	Length of the electrode
$\phi/2\pi$	1/4	Covered ratio by the electrode
R	50 Ω	Input-resistance
G	36.5 dB	Att -3 dB
C	43 pF	Total capacitance of the electrode

from the parameters in Table 2. It is assumed that the longitudinal distribution of particles in a bunch can be expressed by a Gaussian function as follows:

$$I(t) = (qN/\sqrt{2\pi})\sigma \exp(-t^2/2\sigma^2), \quad (4)$$

where q is the particle charge, N is the number of particles in one bunch, and σ is the standard deviation of this Gaussian distribution function. $I(t)$ can be expanded into a Fourier series as

$$I_n = (2qN/T_0) \exp(-n^2\omega_0^2\sigma^2/2), \quad (5)$$

where T_0 is the period of the RF frequency for the RF acceleration cavity and ω_0 is the angular revolution frequency. By using Eq. (2), the coupling impedance Z_n is expressed

$$Z_n = \frac{\phi}{2\pi} \frac{jn\omega_0 R}{(1+jn\omega_0 RC)} \frac{L}{\beta c}, \quad (6)$$

where L is the length of the electrode, βc is the beam velocity, and ϕ is the azimuth angle over which the electrodes cover the beam. The coefficients of the induced voltage (V_n) can then be obtained by

$$V_n = Z_n I_n. \quad (7)$$

Furthermore, the induced voltage as a function of time ($V(t)$) can then be obtained by

$$V(t) = \sum_{n=-\infty}^{\infty} V_n \exp(jn\omega_0 t). \quad (8)$$

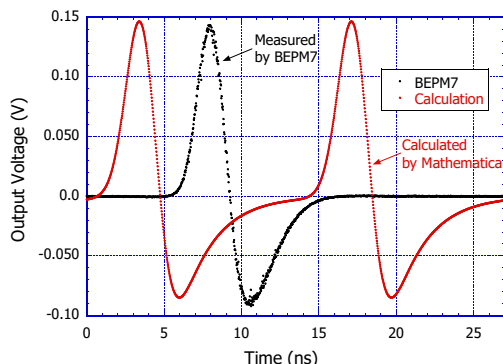


Figure 4: Calculated and measured results of the amplified pickup-voltage in the time domain. Agreement between the measured results and theoretical values is satisfactory.

Figure 4 shows the calculated and measured results of the amplified pickup-voltage in the time domain. The agreement between the measured results and the theoretical values is acceptable. The measured results show only one bunch because the frequency of the pre-accelerator is 36.5 MHz. However, the frequency of the SRILAC is 73 MHz and it has one empty RF bucket. Using the induced voltage V_n from Eq. (7), the pickup-power is given by

$$P_n(\text{dBm}) = 10 \log \left(1000 \times G \text{Att} \frac{1}{R} \left(\frac{V_n}{\sqrt{2}} \right)^2 \right), \quad (9)$$

where G is the gain of the amplifier and Att is the attenuation gain of the coaxial cable, which has a length of about 25.3 m.

Figure 5 shows the theoretically calculated results of the amplified pickup-power in the frequency domain. The parameters used in the calculations are tabulated in Table 2.

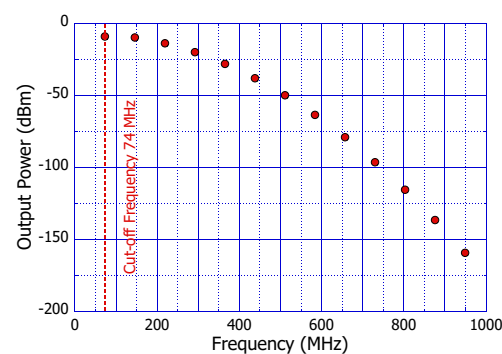


Figure 5: Theoretically calculated results of the amplified pickup-power in the frequency domain.

Improvement of the Noise Figure

We evaluated how a low noise amplifier might improve the noise figure in our system. A noise factor is defined as the ratio between the input S_i/N_i and the output S_o/N_o as follows:

$$F = \frac{S_i/N_i}{S_o/N_o}, \quad (10)$$

where S/N is the signal to noise ratio. When amplifiers are connected in cascade, the total noise factor F_T is expressed as

$$F_T = F_1 + \frac{F_2 - 1}{G_1} + \dots + \frac{F_n - 1}{G_1 \cdot G_2 \cdots G_n} \quad (11)$$

where N_n and G_n are respectively the noise factor and gain of the n -th amplifier. This equation illustrates the important point that the total noise factor is dominated by the performance of the first amplifier, if the amplifier has a high enough gain and low noise floor. Thus, by adapting a low noise amplifier, the total noise factor can be greatly improved. To make the calculation easier, the noise factor is converted to a noise figure (NF) and is expressed in decibels as follows:

$$NF = 10 \log F. \quad (12)$$

The RMS noise voltage V_{nD} of the digitizer PXIE-5160 is 0.14% with a 1-V full-scale range and the band-width is 500 MHz, hence the noise power (P_{nD}) is calculated as fol-

lows:

$$P_{nD} = 10 \log(1000 \times (V_n^2/R)) / (500 \times 10^6) \\ = -131 \text{ dBm/Hz}. \quad (13)$$

Since the thermal noise figure T_N with a resistance of 50Ω at a temperature of 290 K is 174 dBm/Hz, the noise figure NF_D of the digitizer is $174 - 131 = 43$ dB. If an amplifier with a noise figure NF_A of 2.5 dB and a gain G_A of 36.5 dB are connected to the input of the digitizer, the total noise factor F_T is calculated from Eq. (11) as

$$F_T = NF_A + \frac{NF_D - 1}{G_A} = \log^{-1}[2.5/10] + \frac{\log^{-1}[43/10]}{\log^{-1}[36.5/10]} \\ = 6.24. \quad (14)$$

The total noise figure is calculated to be 8.00 dB by using Eq. (12). Finally, we conclude that the improvement of the noise figure is $43 - 8 = 35$ dB/Hz, which yields a great advantage for measurements of weak beams.

Resolution of the Beam Position Measurement

The resolution of the BEPM can be estimated from the total noise figure obtained from the calculation above. Taking into account the bandwidth of 500 MHz, the input noise power P_N is calculated to be $-174 + 8 + 10 \log(500 \times 10^6) = -79$ dBm, which corresponds to be 0.025 mV (rms) of input noise voltage V_N . The resolution of the BEPM is estimated by

$$(\delta x) = (D/2) \times (V_N/V_S), \quad (15)$$

where V_S is the induced voltage on the electrostatic pick-up and D is the diameter of the pick-up. By using 165 mV (rms) (see Fig. 4) for V_S , 0.025 mV for V_N , and 40 mm for D , the resolution δx of the BEPM is evaluated to be 0.003 mm from Eq. (15).

Resolution of the Beam Energy Measurement

To evaluate the resolution of the beam energy measurement, we used the time-of-flight (TOF) method, and took into account the following factors. The length measurement error between each BEPM was $\Delta L = \pm 0.5$ mm, as determined by the accuracy of the laser distance meter, the cable length error was $\Delta T_c = 5$ ps and the error of the zero-crossing point error of the digitizer was $\Delta T_z = 5$ ps. The error in β (the ratio of velocity to light velocity) is expressed as follows:

$$\Delta \beta/\beta = \sqrt{(\Delta L/L)^2 + (\Delta T_c/T_{tof})^2 + (\Delta T_z/T_{tof})^2}. \quad (16)$$

Here, by using a length L of 4.0048 m and TOF T_{tof} of 147 ns, $\Delta \beta/\beta$ is then calculated to be 2.6×10^{-4} . From the relationship $\Delta E/E = 2 \times \Delta \beta/\beta$, we conclude that the absolute resolution of the beam energy is 5.1×10^{-4} . The zero-crossing point is precisely obtained by linearly fitting 50 data points within 1 ns around the zero-crossing point.

Amplifiers and Power Supplies

Figure 6 shows pictures of the customized amplifiers and amplifier power supplies [17] and the data -acquisition system. The specifications of the amplifiers and power supplies

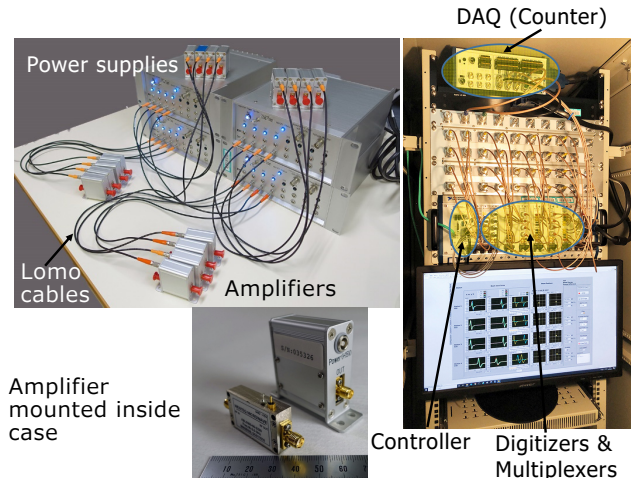


Figure 6: Photographs of the amplifier power supplies, mounted amplifier, and the data -acquisition system (DAQ).

are shown in Table 3. The gains of all the amplifiers are measured in advance and are used by the LabVIEW program for corrections when the beam is measured. The standard de-

Table 3: Electrical Specifications of the Amplifiers and Power Supplies

	Amplifier
Model No.	ABL0300-00-3230 [18]
Bandwidth	9 kHz - 3.0 GHz
Noise Figure	2.5 dB typical, 3.0 dB Max @25 °C
Gain	36.5 dB @25 °C
	Amplifier power supply
Model No.	LFS50A-15 [19]
Output Voltage	15 V
Ripple Noise	10 mV _{p-p}

viation of the gains of all the amplifier's was measured to be 0.15 dB. Lemo conector cables, which can be replaced easily in case of failure, are used to supply power to the amplifiers. The power supplies can be remotely turned on and off with a TTL signal and their statuses are monitored. An LED on the front panel turns on when the amplifier is connected. If the supplied current exceeds 140 ± 20 mA in case of failure, the LEDs turn off and the off-status is returned. For the signal cables, we adopted S 07262 BD coaxial cable [20], which has a significant shielding property and a bandwidth of up to 3 GHz.

Signal Processing System and Programming

A block diagram of the BEPMs and data -acquisition system is shown in Fig. 7 and electrical specifications of the signal processing devices are shown in Table 4. The amplified pickup signals are sent through coaxial cables to the signal processing devices. The upstream and downstream signals are switched by multiplexers and digitized by the digitizers (PXIE-5160). Although the sampling speed is 1.25 GS/s, by using the random interleave mode, a much higher sampling speed of 50 GS/s is available under the

condition that the signal is repeating continuously. As a result, highly accurate TOF measurements can be realized. The random interleave method achieves a higher sampling rate by operating multiple analog-to-digital converters in parallel.

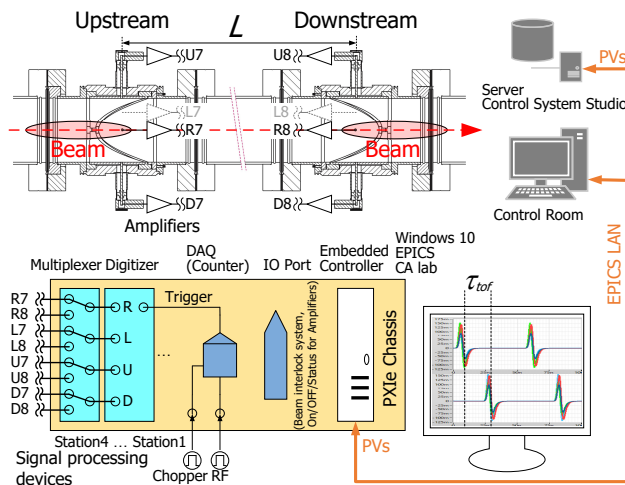


Figure 7: Block diagram of the BEPMs and DAQ.

All the modules are integrated into a PXI express chassis (see Fig. 6). The signal process procedures are controlled by the LabVIEW 2019 graphical programming language and the module drivers are supported by the National Instruments Corporation (Austin, TX, USA) [21]. The obtained data are shared by using CA Lab [22] which is a user-friendly, lightweight, and high performance interface between the LabVIEW program language and the EPICS-based control system. It allows easy reading and writing of EPICS process variables (PV). The BEPM system uses the following PVs: 50 analog inputs, 8 wave-forms, and 13 analog and binary outputs. Currently, measurement results are displayed on a remote desktop. However, once these data are saved, the control system studio, which is an Eclipse-based tool to operate a large-scale control system, can display the results anywhere in the control room.

During the beam tuning procedure, if more than 30 enA of the 0.6 W $^{51}\text{V}^{13+}$ beam [23] is lost, the vacuum pressure becomes rapidly worse, increasing from the 10^{-8} Pa to the 10^{-6} Pa range. To avoid this, the beam current should be attenuated to be as weak as possible to avoid vacuum deterioration during the beam tuning procedure and acceleration trial. Since the upstream signal and down-stream signals are switched by the multiplexer, a reference RF signal is required to measure the TOF of the beam. Furthermore, the RF reference signal also needs to be synchronized with the beam chopper signal, because if the measurement was performed while the beam is being chopped, unnecessary null data would be transferred. To address this issue, we introduced a counter that triggers when it reaches the pre-set RF signal. Figure 8 presents a timing chart showing how the data acquisition is triggered at 30 μs after the chopper signal is launched. Figure 8 presents a timing chart showing how the data acquisition is triggered at 30 μs after the chopper signal is launched.

Here, the 37th counted RF signal just after the chopper signal is launched triggers the digitizers. The counter works

Table 4: Electrical Specifications of the Signal Processing Devices [21]

Embedded Controller (NI PXIE-8840)	
CPU	i7 5700EQ, 2.6 GHz Quad, 8 GB RAM
Transfer rates	8 GB/s
Digitizer (NI PXIE-5160)	
Bandwidth	DC - 500 MHz
Sampling rates	2.5 GS/s (1 ch), 1.25 GS/s (4 ch)
Memory	2 GB
Resolution	10-bit
Channels	4
Transfer rates	600 MB/s
DAQ (NI PXIE-6341)	
IO	16 AI (16-Bit, 500 kS/s), 2 AO, 24 DIO
DAQ (NI PXIE-6612)	
Counter	8-Channel PXI Counter/Time
Multiplexer (NI PXIE-2746)	
Bandwidth	DC - 2.7 GHz
Type	4x1, 4 sets
PXIE Chassis (NI PXIE-1075)	
Slot	18
Transfer rates	4 GB/s

like a field programmable gate array, and the operational procedure is programmed by LabVIEW.

This system is intended to be able to work during SH element searches. The circulating wheel targets are used as shown in Fig. 8; the heavy ion beam is chopped while the target is not irradiated by the beam to avoid radio-activation, temperature increase, and background noise. A photo-sensor detects light emitted through the slit in the wheel frame and creates the chopper signal. Because the BEPM system is synchronized with the chopper signal, precise measurement of the beam position and energy can be realized. Eventually, as beam irradiation of the target continues, some targets

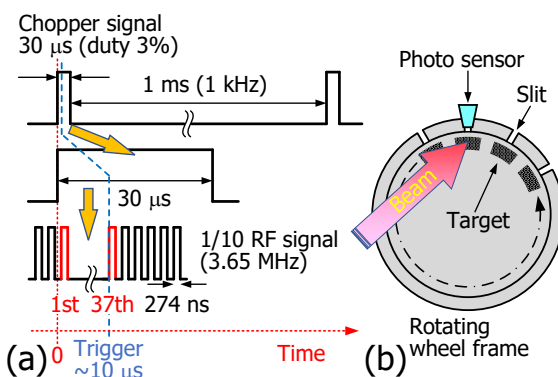


Figure 8: (a) Timing chart showing how the data acquisition is triggered 30 μs after the chopper signal is launched. (b) Circulating wheel target used for the SH element searches. The chopper signal is created by the photo sensor and the slit.

begin to break down. Since the chopper-off signal is manually masked at the broken target position, the synchronized measurement becomes more important. Presently, it is possible to measure the beam position and beam energy at an intensity of 10 enA by chopping the beam to 1/100.

CALIBRATION OF THE BEPMs

With the goal of measuring the beam position to an overall accuracy of ± 0.1 mm, a calibration measurement was performed at the KEK campus in Tokai [24]. A BEPM was connected to a dummy pipe with inner diameter equal to that of one of the BEPMs. Supporting jigs, the dummy pipe, and the BEPM were fixed to an XY stage that could move within the measurement region at 2-mm step intervals. A fixed wire acted as a signal source. If the outputs from the 4 opposing right, left, up, and down electrodes are represented by V_R , V_L , V_U , and V_D , respectively, the horizontal x and vertical y positions of the wire are expressed as follows:

$$\frac{V_R - V_L}{V_R + V_L + V_U + V_D} = \frac{\Delta_x}{\Sigma} \approx f_x(x, y) \approx k_{xx},$$

$$\frac{V_U - V_D}{V_R + V_L + V_U + V_D} = \frac{\Delta_y}{\Sigma} \approx f_y(x, y) \approx k_{yy}. \quad (17)$$

where $f_x(x, y)$ and $f_y(x, y)$ are 5th-order polynomials of the wire (or beam) position and k is a position sensitivity coefficient. The 1st-order approximations of $f_x(x, y)$ and $f_y(x, y)$ are k_{xx} and k_{yy} , respectively.

By using the electrode output voltages V_R , V_L , V_U , and V_D , we calculated the values of Δ_x/Σ and Δ_y/Σ from Eq. (17). By fitting these measured data with a 5th-order polynomial, we calculated $f_x(x, y)$ and $f_y(x, y)$, and obtained the calibration coefficients. In Figs. 9(a) and (b), each calculated wire position is plotted based on the calibration coefficients of 5th-order and 1st-order polynomials, respectively. Although Fig. 9(a) demonstrates that the calculated positions are in fairly good agreement with the wire positions, Fig. 9(b) shows that the data mismatching becomes larger the further away the wire is from the center position. Figure 10(a) (enlarged in 10(c)) shows the residuals between the real wire position and the position obtained from the calibrated 5th-order polynomial and Figure 10(b) shows the residuals from the 1st-order polynomial. These results demonstrate that, the residual of 1σ is less than 10 μ m when we use the 5th-order

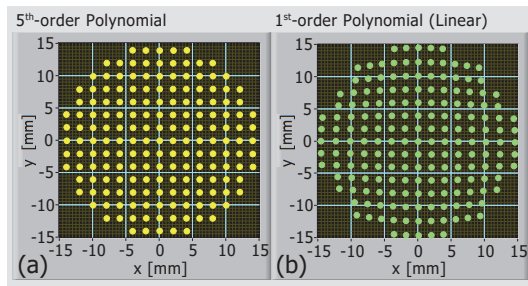


Figure 9: Calculated wire positions plotted by using the calibration coefficients of 5th-order and (b) 1st-order polynomials obtained by the mapping measurements.

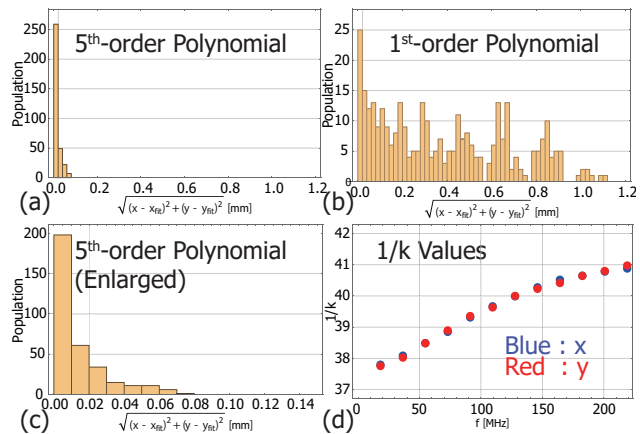


Figure 10: Residuals between the real wire position and the position obtained from the calibrated (a) 5th-order and (b) 1st-order Polynomials. (c) Enlargement of (a). (d) Measured results of the inverse of the position sensitivity coefficients k , which are frequency dependent.

polynomial calibration. In addition, we performed these calibration measurements from 18.25 to 219 MHz in 12 steps of 18.25 MHz intervals. The inverse of the position sensitivity coefficients k of the BEPMs are frequency dependent (Fig. 10(d)). All the 5th-order polynomial calibration coefficients were recorded in tables that the LabVIEW program reads at the time of beam measurement.

COMMISSIONING

Installation of the BEPMs

Since ultrahigh vacuum and particle-free conditions are crucial for SRLAC operation, all the cleaning procedures for the BEPM were done in an ISO class 1 clean room. First, the BEPMs were thoroughly rinsed with ultra-pure water and blow-dried with an ionizing gun [25]. After that, the BEPMs were dried in a vacuum oven at 70°C for 5 days. We continued the blow-drying operation until fewer than 10 particles/s could be detected. Over 3 h was necessary to complete the cleaning procedure for one BEPM. In particular, because long vacuum chambers are present at the ends of the Types I and II BEPMs, they took more time to clean.

To install all the BEPMs between the SRF cavities, half of the quadrupole magnets had to be previously positioned, because the BEPMs were to be installed into their center (Figs. 11(a) and (b)). Since the tolerance between the quadrupole magnet and the BEPM is only 1 mm and strength of the feed-through insulator is very weak against external force, careful adjustment of the installation was carried out with the help of laser transits. It is notable that when we installed the BEPMs, we built a temporary ISO class 1 clean room between the SRF cavities. After the installation, the amplifiers connected to the semi-rigid cables and the stiff coaxial signal cables were securely attached to the end faces of the quadrupole magnets by using specially designed jigs (Fig. 11(c)). The Type III BEPM was designed to be fixed separately on the vacuum chamber (Fig. 11(d)) because it is

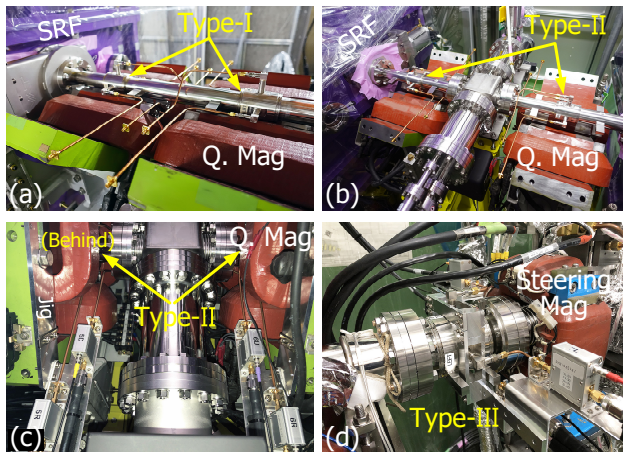


Figure 11: (a) and (b) To install the BEPMs into the center of the quadrupole magnets, half of the quadrupole magnets had to be already previously positioned. (c) and (d) After the installation, the amplifiers connected to the semi-rigid cables and the stiff coaxial signal cables were securely attached.

not installed inside the quadrupole magnet. After installation, we measured the alignment errors from the 32 reference planes; their average was 0.08 mm. Each point alignment error data point was recorded in a file that the LabVIEW program uses to correct the beam position at the time of measurement. To measure the TOF precisely, we adjusted the electrical lengths of the 8 coaxial cable sets, totalling 32 cables, to converge within 3 ps. To adjust the cables, we observed the reflected signal caused by a pulser generator with a rapid 1-ns rise time.

Beam Acceleration by the SRILAC

The first $^{40}\text{Ar}^{13+}$ beam acceleration test was carried out by using the 9 SRF cavities [7]. Figure 12 shows the displayed results of the BEPM measurements just after the beam was successfully accelerated to 6.2 MeV/u (2020/01/28 21:02). The wave-forms, beam positions, and beam energies at each station are displayed; the value circled in red indicates the final accelerated energy.

The measured beam energy is plotted in Fig. 13 as a function of the phase of the final SRF cavity CM3. In the focusing region, the higher energy beam loses energy, whereas in the defocusing region, the lower energy beam gains energy. This measurement clearly shows us which region we should select to accelerate the beam stably. The phases of the SRF cavities are currently set to -25 degrees. Each phase of an SRF cavity was measured and set in sequence from upstream to down-stream.

Figure 14 shows the relationship between the beam position at BEPM 1 and the vacuum between the CM1 and CM2 (see Fig. 1) when the $^{51}\text{V}^{13+}$ beam intensity was increased to 2.5 pA. From this measurement, we recognized that the vacuum rapidly became worse when the beam position shifted from -1 mm to -2 mm. Therefore, we changed the EPICS interlock system to automatically start the beam attenuator to prevent vacuum deterioration.

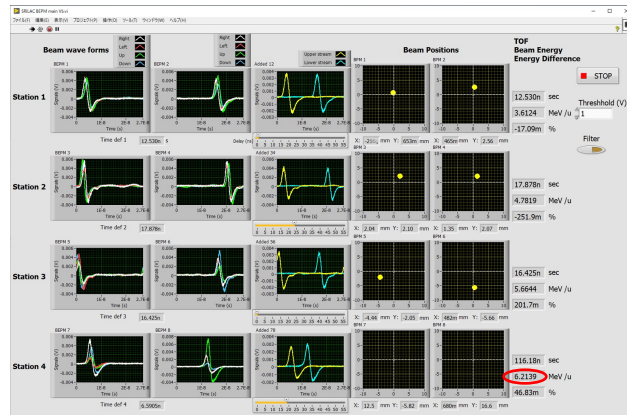


Figure 12: Displayed the BEPM measurement results just after the $^{40}\text{Ar}^{13+}$ beam was successfully accelerated to 6.2 MeV/u (2020/01/28 21:02). The positions at station 4 were off scale, which was corrected after the first trial acceleration.

To obtain beam size information from the BEPMs nondestructively, the quadrupole moments are calculated from the following equation and displayed:

$$Q = k_q \times \frac{V_R + V_L - V_U - V_D}{V_R + V_L + V_U + V_D} - < x >^2 + < y >^2 . \quad (18)$$

Currently, we are comparing the calculations to results from the lattice model to obtain the beam emittances ϵ_x and ϵ_y .

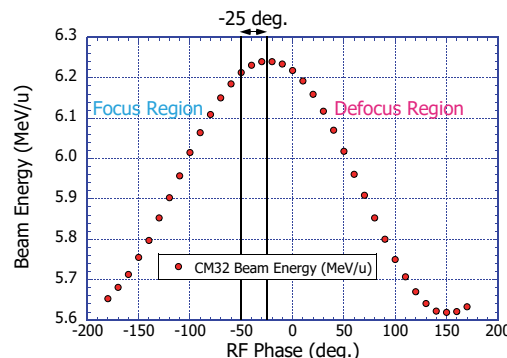


Figure 13: Measured beam energy plotted as a function of the phase of the final SRF cavity CM3.

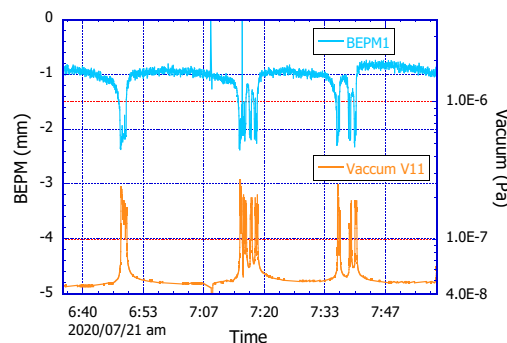


Figure 14: Measured results showing the relationship between the beam position at the BEPM 1 and the vacuum between CM1 and CM2 (see Fig. 1).

CONCLUSION AND FUTURE OUTLOOK

Beam commissioning for the RIKEN Superconducting Linear Accelerator (SRILAC) has been successfully completed. To continually monitor the beam nondestructively, we have developed a new system (BEPM) to determine simultaneously the beam position and energy by measuring the time-of-flight of the beam. The BEPM system worked extremely well in determining the phases of the Superconducting Radio Frequency (SRF) cavities and confirming the beam energies and positions, enabling stable beam acceleration.

We are currently working on measurement of the quadrupole moment to obtain the beam size, the beam intensity from the bunched signal, and the TOF using a lock-in amp technique.

REFERENCES

- [1] K. Morita *et al.*, “New Result in the Production and Decay of an Isotope, $^{278}\text{113}$, of the 113th Element”, *J. Phys. Soc. Jpn.*, vol. 81, 103201, 2012. doi:10.1143/JPSJ.81.103201
- [2] H. Haba, “Production of radioisotopes for targeted radionuclide therapy at RIKEN”, *Drug Delivery System*, vol. 35, no.2, pp. 114-120, 2020. doi:10.2745/dds.35.114
- [3] M. Odera *et al.*, “Variable frequency heavy-ion linac, RILAC: I. Design, construction and operation of its accelerating structure”, *Nucl. Instrum. Methods Phys. Res., Sect. A*, vol. 227, pp. 187–195, 1984. doi:10.1016/0168-9002(84)90121-9
- [4] Y. Yano, “The RIKEN RI Beam Factory Project: A status report”, *Nucl. Instrum. Methods Phys. Res., Sect. B*, vol. 261, pp. 1009–1013, 2007. doi:10.1016/j.nimb.2007.04.174
- [5] H. Okuno *et al.*, “Progress of RIBF accelerators”, *Prog. Theor. Exp. Phys.*, vol. 2012, p. 03C002, 2012. doi:10.1093/ptep/pts046
- [6] T. Nagatomo *et al.*, “New 28-GHz Superconducting ECR Ion Source for Synthesizing New Super Heavy Elements of $Z > 118$ ”, in *Proc. ECRIS'18*, Catania, Italy, Sep 2018, pp. 53–57. doi:10.18429/JACoW-ECRIS2018-TUA3
- [7] N. Sakamoto *et al.*, “Development of Superconducting Quarter-Wave Resonator and Cryomodule for Low-Beta Ion Accelerators at RIKEN Radioactive Isotope Beam Factory”, in *Proc. SRF'19*, Dresden, Germany, Jul. 2019, pp. 750-757. doi:10.18429/JACoW-SRF2019-WETEB1
- [8] H. Imao *et al.*, “Non-Evaporative Getter-Based Differential Pumping System for SRILAC at RIBF”, in *Proc. SRF'19*, Dresden, Germany, Jul. 2019, pp. 419-423. doi:10.18429/JACoW-SRF2019-TUP013
- [9] T. Watanabe *et al.*, in *Proc. of the 15th Annual Meeting of Particle Accelerator Society of Japan*, Aug. 2018, pp. 49-54; http://www.pasj.jp/web_publish/pasj2018/proceedings/index.html
- [10] TOYAMA Co., Ltd., <http://www.toyama-en.com/>
- [11] G. Nassibian, “The measurement of the multipole coefficients of a cylindrical charge distribution”, CERN-SI-NOTE-EL-70-13, 1970. <http://cds.cern.ch/record/358718>
- [12] Ferrotec Material Technologies Co., <http://www.ft-ceramics.co.jp/en/>
- [13] MARUWA Co., Ltd., <https://www.maruwa-g.com/e/>
- [14] Robert E. Shafer, “Beam position monitoring”, *AIP Conference Proceedings*, vol. 249, p. 601, 1992. doi:10.1063/1.41980
- [15] T. Watanabe *et al.*, “Beam position monitoring system and COD correction at the cooler synchrotron TARN II”, *Nucl. Instrum. Methods Phys. Res., Sect. A*, vol. 381, p. 194, 1996. doi:10.1016/S0168-9002(96)00528-1
- [16] T. Watanabe *et al.*, “Development of beam energy and position monitor system at RIBF”, in *Proc. of the 14th Annual Meeting of Particle Accelerator Society of Japan*, Aug. 2017, paper WEP091, pp. 1112-1117. http://www.pasj.jp/web_publish/pasj2017/proceedings/PDF/WEP0/WEP091.pdf
- [17] Hayashi-Repic Co., <https://www.h-repic.co.jp/>
- [18] Wenteq Microwave Co., <http://www.wenteq.com/>
- [19] Daitron Co., <http://www.daitron.co.jp/en/>
- [20] Huber+Suhner AG, <https://www.hubersuhner.com/en>
- [21] National Instruments Corp., <http://www.ni.com/>
- [22] BESSY CA Lab, https://www.helmholtz-berlin.de/zentrum/locations/it/software/exsteuer/calab/index_en.html
- [23] Y. Higurashi *et al.*, RIKEN Accel. Prog. Rep., vol. 51, p. 17, 2018.
- [24] T. Watanabe *et al.*, “Calibration for Beam Energy Position Monitor System for Riken Superconducting Acceleration Cavity”, in *Proc. IBIC'19*, Sept. 2019, pp. 526-529. doi:10.18429/JACoW-IBIC2019-WEPP007
- [25] SIMCO ION, <http://www.simcoion.jp/>